RSC Advances

PAPER

View Article Online
View Journal | View Issue

Cite this: *RSC Adv.*, 2025, **15**, 14363

Enhanced fluoride removal from drinking water by activated carbon supported Ce–Al oxides: performance and mechanism†

Shaoying Guo,[a] Fuwang Zheng,[b] Junchao Xu,[b] Juan Jiang,[d] Zhou Cui,[c] Chunshan Wu,[b] Yilong Lin,[e] Qiyuan Sun,[b] Yuyi Zheng*[b] and Baisheng Sa*[c]

Elevated fluoride levels in drinking water pose a significant challenge to human health, necessitating affordable and effective adsorbents for fluoride removal. This study presents the synthesis of a Ce–Al binary metal oxide composite adsorbent supported on activated carbon (Ce–Al–O/AC) for the defluoridation of drinking water. The adsorbent, employing the synergistic bimetallic effect, demonstrates robust fluoride removal performance across a wide pH range of 4–10. It is worth highlighting that the equilibrium adsorption capacity reaches 17.97 mg g^{-1} at 298 K and pH 6 within 2 h, utilizing an adsorbent dose of 0.5 g L^{-1} in an initial 10 mg L^{-1} fluoride solution. The phosphate exerts the most significant influence on the defluoridation efficiency. The adsorption kinetics and isotherms align with the pseudo-second-order kinetics model and Langmuir isotherm model, respectively. Moreover, the defluoridation process is characterized as spontaneous and endothermic, with a maximum adsorption capacity of 31.65 mg g^{-1} at 298 K. Further experimental and theoretical evidences reveal that fluoride adsorption is primarily driven by electrostatic interactions and ion exchange. The dynamic adsorption tests coupled with economic analyses highlight the promise of Ce–Al–O/AC as a cost-effective and efficient adsorbent for practical drinking water defluoridation.

Received 16th January 2025
Accepted 25th April 2025

DOI: 10.1039/d5ra00397k

rsc.li/rsc-advances

1. Introduction

Elevated fluoride levels in drinking water is a serious regional issue around the world. Excessive intake over time can lead to detrimental effects such as dental fluorosis, skeletal fluorosis, and diseases of the neurological and endocrine systems.[1,2] So far, fluoride-induced human poisoning has affected over 50 countries around the world, with more than 260 million people suffering from fluorosis, including 22 to 45 million people in China.[3] Therefore, China has stipulated a drinking water standard whereby the fluoride concentration should not exceed 1.0 mg L^{-1}, making the strict control of fluoride concentration in drinking water a critical issue.

A variety of techniques have been developed to remove fluoride from water, including chemical precipitation,[4] membrane separation,[5] ion exchange[6] and adsorption.[7] Among these techniques, adsorption stands out as an economical and efficient method, noted for its low cost, simplicity, and high removal efficiency.[8] Many different adsorbents have been investigated for their ability to remove fluorides, such as biomaterials,[9] natural minerals,[7,10] metal materials,[11] carbon materials,[12] and metal–organic frameworks (MOFs).[13,14] Carbon materials,[15,16] especially activated carbon, are favored for their cost-effectiveness, high surface area, and well-developed pore structure.[17] However, the use of activated carbon alone for the removal of inorganic anions like fluoride is not effective, and modification with various additives is also required.[12] Metal oxides and hydroxides exhibit a strong affinity for fluoride ions, prompting extensive research on the modification of activated carbon with various metal compounds such as calcium,[18] aluminum,[19] iron,[20] magnesium,[12,21] stannum,[22] zirconium[23] and lanthanum[24] to enhance their defluoridation capacities. Previous studies have shown that bimetallic oxides exhibit superior fluoride removal abilities compared to their single metal oxide counterparts owing to the synergistic effects.[25] Notably, aluminum oxide is a commonly used and effective fluoride remover,[19] and among rare earth metal oxides, cerium oxide is relatively inexpensive and readily available compared to lanthanum oxide. Particularly, cerium oxide possesses distinct

[a]*School of Pharmacy, Fujian Health College, Fuzhou 350101, China*
[b]*College of Environmental and Resource Sciences, Fujian Normal University, Fujian Key Laboratory of Pollution Control & Resource Reuse, Fujian College and University Engineering Research Center for Municipal Waste Resourceization and Management, Fuzhou 350007, China. E-mail: zhengyy@fjnu.edu.cn*
[c]*Multiscale Computational Materials Facility & Materials Genome Institute, School of Materials Science and Engineering, Fuzhou University, Fuzhou 350108, China. E-mail: bssa@fzu.edu.cn*
[d]*Fujian Xiamen Environmental Monitoring Center Station, Xiamen 361022, China*
[e]*Fuzhou Research Academy of Environmental Science, Fuzhou 350011, China*

† Electronic supplementary information (ESI) available. See DOI: https://doi.org/10.1039/d5ra00397k

and favorable properties, such as variable oxidation states and higher ionic size.[26] Moreover, previous studies have demonstrated that the incorporation of Ce in composite adsorbents can promote the formation of hydroxyl groups, which are beneficial for fluoride adsorption.[27,28]

Therefore, a Ce–Al–O/AC composite adsorbent for drinking water defluoridation was synthesized in this study. Key effect factors included solution pH, initial fluoride concentration, coexisting ions, adsorption time, and temperature on fluoride removal efficiency were thoroughly studied as well as the rules of adsorption kinetics, adsorption isotherm, and thermodynamics were also explored. Combined with the results of characterization, static adsorption experiments, and DFT calculations, the defluoridation mechanisms of Ce–Al–O/AC were comprehensively elucidated. In addition, its practical application viability was certified by dynamic adsorption test and economic analysis. The results indicate that it serves as an economical and effective adsorbent for practical application in drinking water defluoridation.

2. Materials and methods

2.1. Chemicals

All chemicals in this study were obtained from commercial sources and were not further purified. The activated carbon (AC) was purchased from Lvzhiyuan Co., Ltd. Cerium nitrate ($Ce(NO_3)_3 \cdot 6H_2O$) was purchased from Sinopharm Chemical Reagent Co., Ltd. Aluminum chloride ($AlCl_3 \cdot 6H_2O$) and ammonia ($NH_3 \cdot H_2O$) were purchased from Xilong Science Co., Ltd.

2.2. Adsorbents preparation

The composite adsorbent was synthesized by the co-precipitation method. To determine the optimization of metal molar ratio in bimetallic oxides, samples with different Al/Ce molar ratios were prepared. The preparation of activated carbon supported Ce–Al oxides was similar to bimetallic oxides. The preparation and optimization preparation conditions for defluoridation of adsorbents were recorded in the ESI.† Moreover, as Ce salts are relatively more expensive than Al salts, considering performance comparison and economic factors, the adsorbents were synthesized in the same way at calcined at 203 °C for 200 min with $n(Al)/n(Ce) = 0:0$, $0:1$, $14:3$, respectively. The adsorbents above were denoted as AC, Al–O/AC, and Ce–Al–O/AC, respectively. And the Ce–Al–O/AC after adsorption was denoted as Ce–Al–O/AC–F.

2.3. Characterization methods

The surface morphology and element distribution of AC, Al–O/AC, Ce–Al–O/AC, and Ce–Al–O/AC–F were gained by scanning electron microscope (SEM, Regulus 8100, Japan) equipped with an energy dispersive spectroscopy (EDS, Octane elect plus, USA). The specific surface area and pore size distribution of the adsorbents were measured by the surface area and porosity analyzer (BET, BELSORP-Mini II, Japan). The structural characteristics of carbonaceous materials can be characterized by a Raman spectrometer (Raman, Thermo Scientific, USA). The crystallinity and phase structure of materials were determined by X-ray diffraction (XRD, D8 Advance, Germany). The surface functional groups of AC, Al–O/AC, Ce–Al–O/AC, and Ce–Al–O/AC–F were analyzed qualitatively by Fourier transform infrared spectroscopy (FT-IR, Nicolet iS10, USA). The binding energy, elemental composition, and oxidation state of the adsorbents were determined by an X-ray photoelectron spectrometer (XPS, ESCALAB 250, USA).

2.4. Adsorption experiment

Under the conditions of 10 mg adsorbent dosage, 298 K temperature, and 120 min adsorption time in 20 mL fluorine-containing solution, the defluoridation performances of the aforementioned adsorbents were investigated; key parameters included different pH values, initial fluoride concentration, and the influence of coexisting ions on fluoride removal efficiency. All adsorption experiments were performed in a shaker at 150 rpm. For kinetics studies, 10 mg of Ce–Al–O/AC was introduced to 10 mg L^{-1} fluoride solution. For thermodynamics studies, 10 mg of Ce–Al–O/AC was added to fluoride solution with varying initial fluoride concentrations (10 mg L^{-1} to 80 mg L^{-1}) at different temperatures (288 K, 298 K, 308 K, and 318 K).

In addition, the fixed-bed experiments were conducted by adding 3.0 g of Ce–Al–O/AC respectively within dynamic adsorption plastic columns (12.8 mm in inner diameter and 115 mm in length). The fluoridated drinking water (water quality shown in Table S1†) was injected at different constant flow rates by the peristaltic pump (BT100S-1, China).

The fluoride concentration in the solution was determined by the fluoride ion electrode method. All experiments were performed in duplicate. The fluoride equilibrium adsorption capacity q_e (mg g^{-1}) and the removal rate η_e (%) are calculated as follows:

$$q_e = \frac{(C_0 - C_e)V}{m} \quad (1)$$

$$\eta_e = \frac{(C_0 - C_e)}{C_0} \times 100\% \quad (2)$$

Here, C_0 (mg L^{-1}) and C_e (mg L^{-1}) are the initial and equilibrium concentrations of fluoride before and after adsorption. The m (mg) and V (mL) represent the weight of the adsorbents and the volume of the solution, respectively.

2.5. Computational details

The density functional theory (DFT) based theoretical calculations of the adsorption configurations were implemented in the QuantumWise Atomistix ToolKit (Quantum ATK) package.[29] The GGA-PBE functional with a linear combination of atomic orbitals (LCAO) norm-conserving PseudoDojo pseudopotential[30] was employed to deal with the electron exchange and correctional interactions. The valence electrons were expanded using a numerical atomic-orbital basis set of double-zeta polarization (DZP) for all atoms.[31] To prevent interaction

between adjacent layers, a vacuum space of 20 Å was inserted along the z direction. The cutoff energy of 125 hartree and the Monkhorst k-point mesh of $3 \times 3 \times 1$ were applied to the calculations of optimization and the calculations of adsorption energy. The ion adsorption configurations took the DFT-D3 correction method into account.[32,33] The convergence criterion of the force was set to 0.02 eV $Å^{-1}$.

3. Results and discussion

3.1. Defluoridation performance of different absorbents

The defluoridation capacity of metal oxides at different Al/Ce molar ratios is displayed in Fig. 1(a). It can be observed that the fluoride removal performance of Ce oxide is inferior to that of Al oxide. The defluoridation of Ce–Al bimetallic oxides with different Al/Ce ratios is superior to that of Ce oxide and Al oxide alone, with the optimal fluoride removal performance at an Al/Ce ratio of 4 : 1. Thus, it can be speculated that a synergistic effect occurs between Ce oxide and Al oxide and the specific structure facilitated for defluoridation is formed in the Ce–Al bimetallic oxides composites. These results are consistent with other studies.[34]

Based on this foundation, activated carbon supported Ce–Al oxides were prepared, and the preparation process was optimized by the response surface methodology (RSM) method. The results of the interaction of the preparation conditions are presented in Fig. S1.† The optimal preparation conditions were determined to be the calcination temperature of 203 °C, the calcination time of 3.33 h, and the Al/Ce molar ratio of 14 : 3. The composite absorbent prepared under these optimal conditions was designated as Ce–Al–O/AC. The fluoride removal performance of AC, Al–O/AC, and Ce–Al–O/AC is shown in Fig. 1(b). It indicates that the Ce–Al–O/AC achieves an adsorption capacity of 17.97 mg g^{-1}, which is notably higher—twice and sixteen times than those of Al–O/AC composite materials and AC alone, respectively. This significant enhancement in defluoridation ability owing to their synergistic effect of aluminum and cerium oxides supported on activated carbon. Therefore, an in-depth investigation into the characterization and defluoridation influencing factors of Ce–Al–O/AC is necessary.

3.2. Characterization of materials

The SEM images and EDS images of materials are shown in Fig. 2. It can be found that Al–O/AC, Ce–Al–O/AC, and Ce–Al–O/AC–F all retain the porous structure characteristic of activated carbon. By contrast, more abundant irregular particles, identified as metal oxides resulting from high-temperature calcination of the composite samples, are observed on the surfaces and within pores of Al–O/AC and Ce–Al–O/AC.[35] EDS analysis of Ce–Al–O/AC (Fig. 2(e–i)) and EDS data comparisons with AC and Al–O/AC (Table S2†), confirm the successful adherence of cerium and aluminum on its surface, with O distribution coinciding with that of Ce and Al, and some overlap between Ce and Al. Furthermore, from the EDS images of Ce–Al–O/AC–F (Fig. 2(j–n)), it can be seen that F overlaps highly with O. Considering the relationship between O and Ce, Al reflected by the EDS of Ce–Al–O/AC, it is evident that the Ce–Al bimetallic oxide system plays a synergistic role in the fluoride adsorption process.

N_2 adsorption–desorption isotherms and BJH desorption pore size distributions for AC, Al–O/AC, and Ce–Al–O/AC are depicted in Fig. 3. According to the IUPAC classification, the N_2 adsorption isotherms for these materials exhibit both Type I and IV characteristics, indicating the coexistence of micropores and mesopores. Besides, their hysteresis loops, classified as type H4, lack distinct saturated adsorption plateaus, illustrating irregular slit-like pore structures. The specific surface area, pore volume, and pore diameter of the AC, Al–O/AC, and Ce–Al–O/AC are summarized in Table S3.† Notably, while Ce–Al–O/AC has a reduced specific surface area (330.50 $m^2 g^{-1}$) compared to AC (487.07 $m^2 g^{-1}$) and Al–O/AC (470.41 $m^2 g^{-1}$), it shows superior defluoridation performance in the previous test. It suggests that chemical adsorption may be more influential than physical adsorption in Ce–Al–O/AC's fluoride uptake, a hypothesis that needs further confirmation.

In Fig. 4(a), the peaks near 1340 cm^{-1} and 1590 cm^{-1} are both observed in the Raman spectra of AC, Al–O/AC, and Ce–Al–O/AC, which correspond to the D and G bands respectively.[36] According to the strength ratio (I_D/I_G) of the D and G bands recorded in Table S4,† the I_D/I_G values of Al–O/AC and Ce–Al–O/AC are relatively larger, indicating the greater degree of structural defects compared to AC. Previous studies[36] have

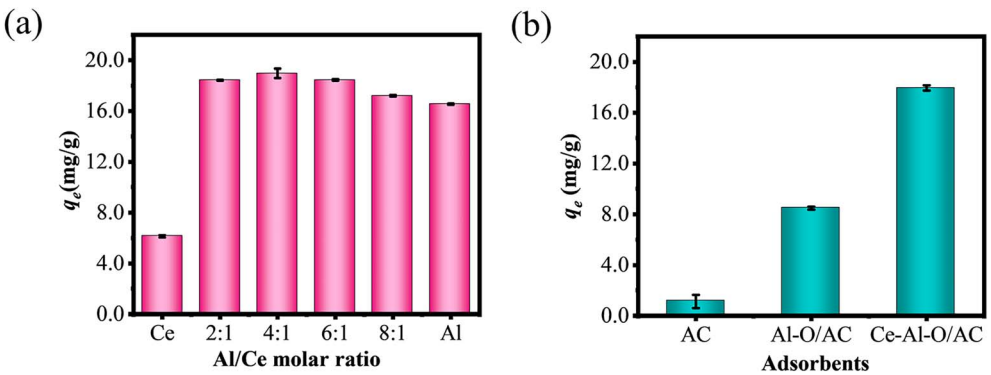

Fig. 1 The defluoridation capacity of (a) metal oxides at different Al/Ce molar ratios, (b) AC, Al–O/AC and Ce–Al–O/AC (dose = 0.5 g L^{-1}, C_0 = 10 mg L^{-1}, t = 120 min, T = 298 K).

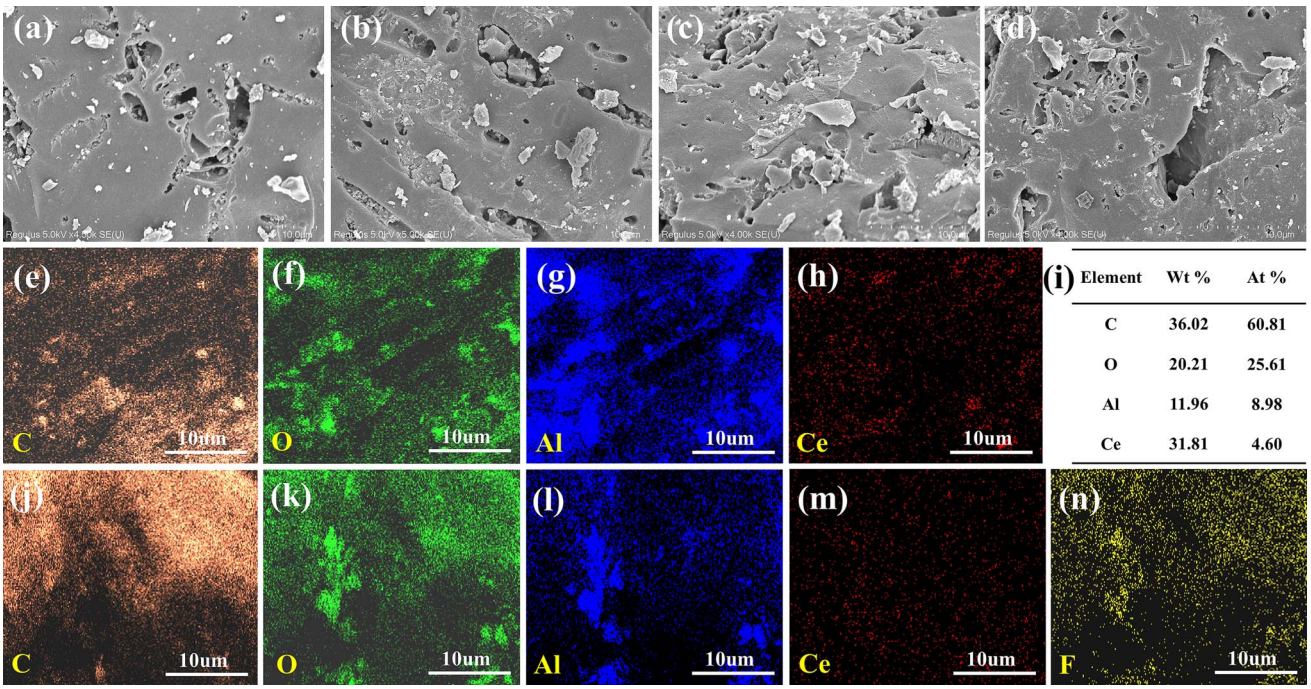

Element	Wt %	At %
C	36.02	60.81
O	20.21	25.61
Al	11.96	8.98
Ce	31.81	4.60

Fig. 2 SEM images of (a) AC, (b) Al–O/AC, (c) Ce–Al–O/AC, and (d) Ce–Al–O/AC–F, EDS images of (e–i) Ce–Al–O/AC and (j–n) Ce–Al–O/AC–F.

demonstrated that the defect structures of carbonaceous materials and the supported metal oxides could be acted as active sites for adsorbents, which results in the superior defluoridation performance of Al–O/AC and Ce–Al–O/AC. Additionally, the D and G bands in the Raman spectrum of Ce–Al–O/AC are broader than those of Al–O/AC. It suggests that the Ce–Al–O/AC composite adsorbent is not a mere mixture of Ce oxide and Al oxide on activated carbon, but possesses a higher density of defects and a lower degree of graphitization, which can lead to enhancing chemical adsorption.

As shown in Fig. 4(b). The XRD pattern of AC exhibits a broad diffraction peak of amorphous structure.[37] In the XRD spectrum of Ce–Al–O/AC, characteristic peaks of CeO_2 are observed at 2θ positions of 28.542°, 33.075°, 47.475°, 56.332°, and 76.685° (JCPDS: 01-081-0792), corresponding to crystal planes (111), (200), (220), (311), and (331).[38–40] Whereas, no crystalline aluminum oxides are displayed in the XRD pattern of Ce–Al–O/AC and Al–O/AC, indicating that most of the aluminum oxide compounds are present in an amorphous state on the surface of absorbents.[41] In the XRD spectrum of Ce–Al–O/AC–F, the characteristic peak intensity of CeO_2 is significantly reduced. It can be inferred that CeO_2 is involved in the process of adsorbing fluoride.[42]

The FTIR spectra of AC, Al–O/AC, Ce–Al–O/AC, and Ce–Al–O/AC–F are shown in Fig. 4(c). All samples display broad peaks at 1080 cm^{-1} and 3430 cm^{-1}, indicating the stretching vibrations of the C–O bond and –OH from interlayer water molecules (H–O–H).[43] The weaker peaks at 2920 cm^{-1} and 1580 cm^{-1} are assigned to the stretching vibrations of the $-CH_2-$ and C=C bonds.[44] In comparison with AC, the FTIR spectrum of Al–O/AC and Ce–Al–O/AC reveal three new peaks at 1390 cm^{-1}, 700 cm^{-1}, and 580 cm^{-1}, corresponding to the bending vibration of

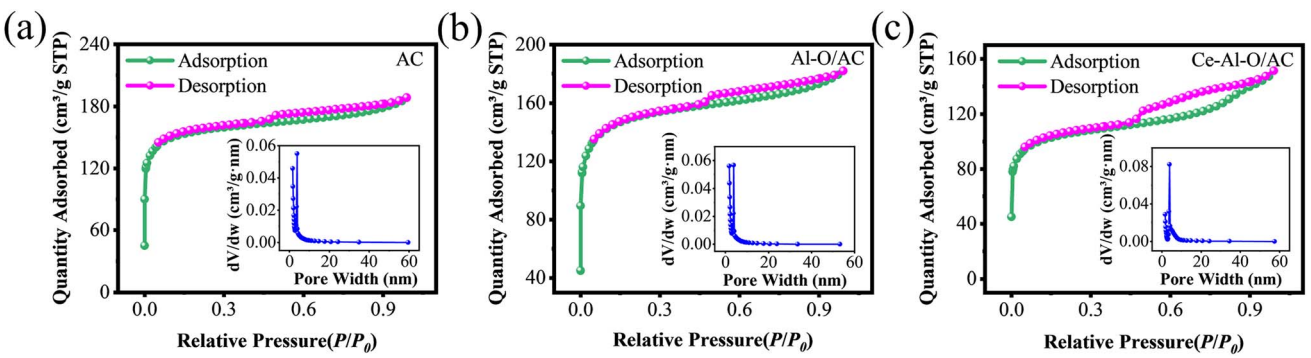

Fig. 3 N_2 adsorption–desorption isotherms and BJH pore size distribution curves of (a) AC, (b) Al–O/AC, and (c) Ce–Al–O/AC.

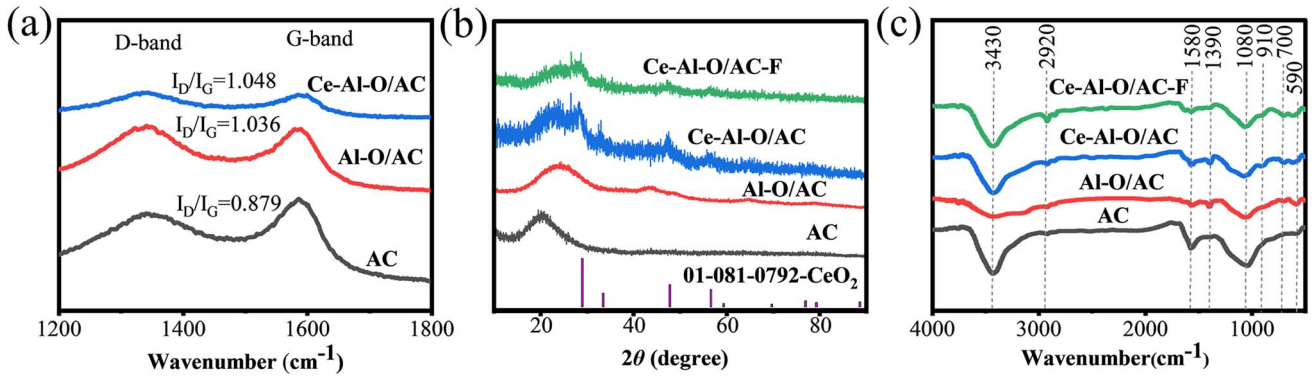

Fig. 4 (a) Raman spectra of AC, Al–O/AC, and Ce–Al–O/AC, (b) X-ray patterns of AC, Al–O/AC, Ce–Al–O/AC, and Ce–Al–O/AC–F, (c) the FTIR spectra of AC, Al–O/AC, Ce–Al–O/AC, and Ce–Al–O/AC–F.

hydroxyl groups and the bending and symmetric stretching vibration of Al–O–Al metal bonds, respectively.[45] Additionally, another distinctive peak at 910 cm^{-1} in Ce–Al–O/AC is assigned to the Ce–O bond.[26,46] Interestingly, after adsorption, the peak intensities of Ce–Al–O/AC–F at 1390 cm^{-1} and 910 cm^{-1} markedly decrease, indicating that the fluoride adsorption by Ce–Al–O/AC involves interactions with hydroxyl groups and cerium oxides.

3.3. Adsorption study of Ce–Al–O/AC

Fig. 5(a) illustrates that Ce–Al–O/AC exhibits relatively high fluoride adsorption efficiency across a wide pH range of 4–10, demonstrating its adaptability for drinking water conditions. The adsorption efficiency reaches the peak at a solution pH of 6, while the pH_{pzc} of Ce–Al–O/AC is 10.98 (Fig. S2†), suggesting that electrostatic adsorption is not the sole defluoridation pathway. The low adsorption efficiency observed at pH 3–4 is ascribed to the gradual conversion of F^- to HF in highly acidic solutions (Fig. S3†), which reduces the ease of removal by either electrostatic adsorption or substitution by OH on the adsorbent surface.[26] Conversely, as the pH increases from 6 to 10, the tiny reduction in positive surface charge hinders the absorption of F^- onto the active sites and emerges competitive chemisorption between hydroxide ions and F^-. At a solution pH of 11, the Ce–Al–O/AC surface carries a negative charge, resulting in electrostatic repulsion with F^- and increased competition for adsorption with hydroxyl ions in the solution.[26]

As shown in Fig. 5(b), with the increase of initial fluoride concentration from 10 to 80 mg L^{-1}, the fluoride removal capacity of Ce–Al–O/AC increases from 17.97 mg g^{-1} to 31.03 mg g^{-1}, but the fluoride removal efficiency decreases from 89.16% to 19.39%. That can be due to an increase in the adsorption driving force and a decrease in the resistance of adsorption at high fluoride initial concentrations.[47] This trend aligns with findings from other studies.[48]

The competitive effect of co-existing anions on the removal performance of fluoride is shown in Fig. 5(c). The influence of these ions on fluoride is ranked as follows: PO_4^{3-} > CO_3^{2-} > SO_4^{2-} > NO_3^- > Cl^-, mirroring results from other studies.[48] In particular, PO_4^{3-} exerts the greatest effect on fluoride removal. The results reveal that multivalent anions, characterized by higher charge densities, are preferentially adsorbed onto positively charged adsorbent surfaces than monovalent anions.[49]

As shown in Fig. S4(a),† the fluoride adsorption of Ce–Al–O/AC reaches equilibrium after 2 h, but the adsorption capacity at 15 min is up to 17.04 mg g^{-1}, which is 94.8% of the equilibrium adsorption capacity. The fast adsorption rate of Ce–Al–O/AC in

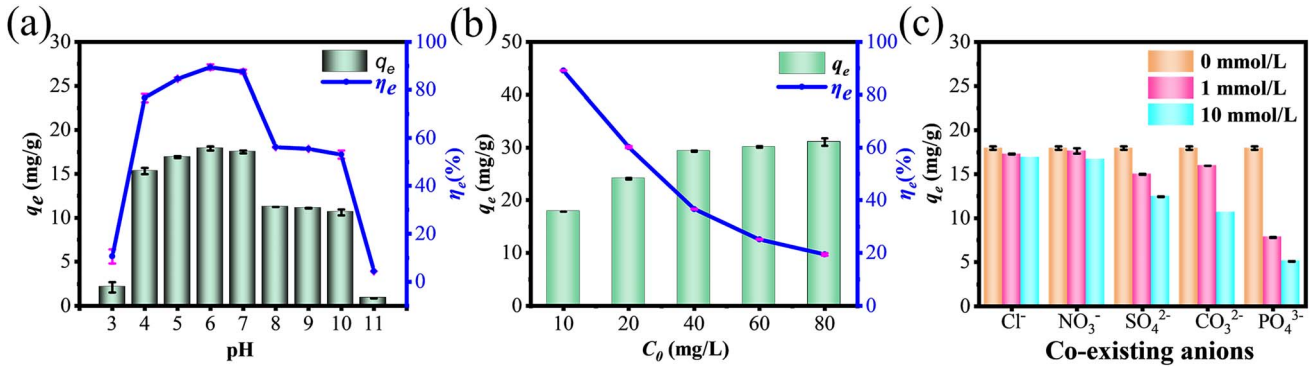

Fig. 5 Effect of (a) solution pH (dose = 0.5 g L^{-1}, C_0 = 10 mg L^{-1}, t = 120 min, T = 298 K), (b) initial fluoride concentration (dose = 0.5 g L^{-1}, pH = 6, t = 120 min, T = 298 K) and (c) co-existing anions (dose = 0.5 g L^{-1}, C_0 = 10 mg L^{-1}, pH = 6, t = 120 min, T = 298 K) on fluoride removal by Ce–Al–O/AC.

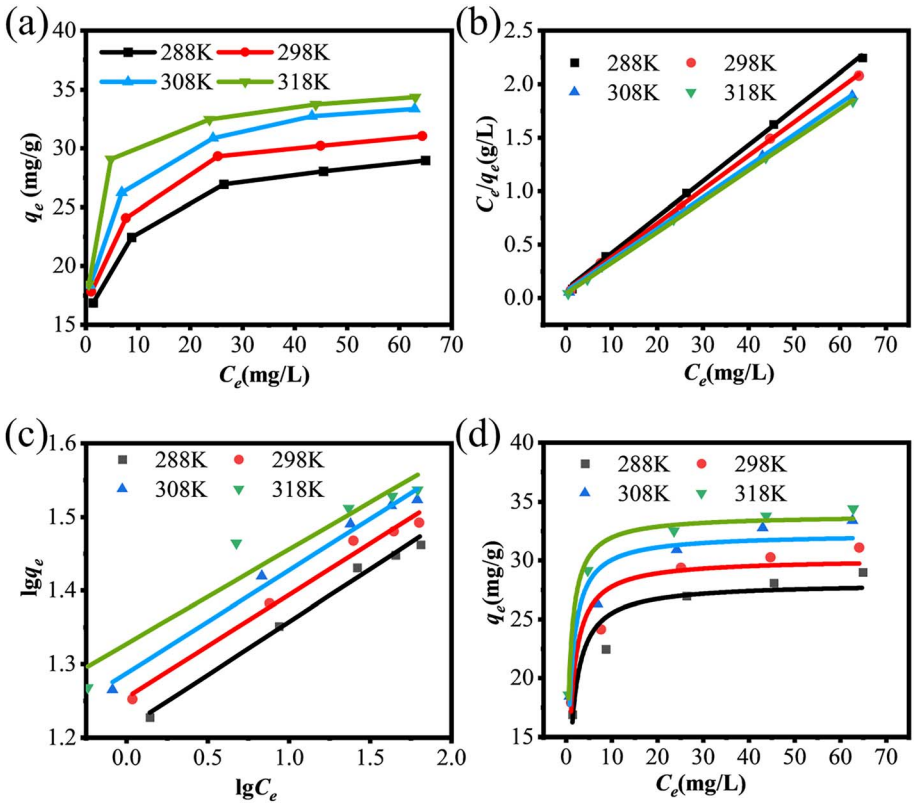

Fig. 6 (a) Fluoride adsorption isotherms of Ce–Al–O/AC at different temperatures (dose = 0.5 g L^{-1}, pH = 6, t = 120 min, C_0 = 10–80 mg L^{-1}), (b) Langmuir, (c) Freundlich, and (d) DR isotherms of fluoride adsorption.

the first 15 min is mainly due to the large number of adsorption sites in the initial stage. Subsequently, the active sites are progressively occupied until they reach the adsorption capacity saturation.[48] To study the adsorption kinetics, pseudo-first-order, pseudo-second-order, and intra-particle diffusion models (recorded in the ESI†) were used to fit with the experimental data (shown in Fig. S4(b)–(d)†). Comparing the summarized parameters of the tree models in Table S5† shows that the pseudo-second-order model (R^2 = 0.9999) is much better fitted with the adsorption process than the pseudo-first-order model (R^2 = 0.8248) and intra-particle diffusion model (R^2 = 0.8811–0.9967), suggesting that the chemisorption would be the main process of fluoride adsorption by Ce–Al–O/AC.[50,51]

Fig. 6 illustrates the adsorption results of Ce–Al–O/AC for fluoride ions at different temperatures and fluoride concentrations. According to Fig. 6(a), as the temperature increases from 288 K to 318 K, the saturated adsorption capacity (q_e) of Ce–Al–O/AC for fluoride gradually rises from 28.98 mg g^{-1} to 34.37 mg g^{-1}, demonstrating that the adsorption reaction is an endothermic process. Fig. 6(b–d) illustrate the analysis of the q_e of defluoridation by Ce–Al–O/AC at different temperatures using Langmuir, Freundlich, and Dubinin Radushkevich (D–R) isotherm models. All fitting parameters are presented in Table S6.† Compared with the Freundlich model (R^2 = 0.9213–0.9902) and the D–R model (R^2 = 0.9027–0.9870), the Langmuir model (R^2 = 0.9991–0.9997) shows a better fit with the experimental data, reflecting that the adsorption process of Ce–Al–O/AC is attributed to mono-layer adsorption.[13] In addition, the max defluoridation capacity of Ce–Al–O/AC calculated by the Langmuir model is 31.65 mg g^{-1} at ambient temperature. The

Table 1 Comparison of maximum adsorption capacities of different adsorbents

Adsorbents	q_{max} (mg g^{-1})	React condition	Dose (g L^{-1})	References
Ce–Al–O/AC	31.65	C_{F^-} = 10–80 mg L^{-1}, pH = 6, T = 298 K, t = 2 h	0.5	This work
AC–CMCSL	2.01	C_{F^-} = 2–25 mg L^{-1}, pH = 7, T = 298 K, t = 1.67 h	10	18
AC–Al	13.03	C_{F^-} = 5–30 mg L^{-1}, pH = 6.15, T = 298 K, t = 1 h	1.5	19
AIAABC	21.1	C_{F^-} = 5–30 mg L^{-1}, pH = 7, T = 298 K, t = 3 h	0.8	20
MPCC	26.6	C_{F^-} = 10–35 mg L^{-1}, pH = 7, T = 298 K, t = 70 min	2.0	21
SnO_2–AC	4.56	C_{F^-} = 2–10 mg L^{-1}, pH = 6, T = 293 K, t = 24 h	0.28	22
Zr–ACF	28.50	C_{F^-} = 10–80 mg L^{-1}, pH = 7, T = 298 K, t = 6 h	2.0	23
MAC–La	12.178	C_{F^-} = 1–48 mg L^{-1}, T = 298 K, t = 24 h	1.2	24

parameter R_L in the Langmuir model is between 0 and 1, and the parameter n in the Freundlich model is greater than 1, which indicates that the fluoride adsorption process is advantageous.[13] The free energy (E) values calculated *via* the D–R model at various temperatures all exceed 16 kJ mol^{-1}, indicating that the adsorption of fluoride by Ce–Al–O/AC is predominantly chemical adsorption.[52] Thermodynamic parameters are summarized in Table S7,† with fitting results depicted in Fig. S5.† The negative ΔG values across the tested temperatures confirm the spontaneity of fluoride adsorption. The positive ΔH (11.5385 kJ mol^{-1}) and ΔS (0.1614 kJ mol^{-1}) values reveale that the adsorption process is endothermic and increases the disorder of the system.[13,50]

3.4. Defluoridation performance evaluation of Ce–Al–O/AC

Table 1 shows the comparison of defluoridation performance of Ce–Al–O/AC with other adsorbents in previous studies. It can be seen that the maximum defluoridation capacity of Ce–Al–O/AC is up to 31.65 mg g^{-1}, which is much higher than other adsorbents with lower dosages. This indicates the superiority of its defluoridation performance.

3.5. Mechanism analysis

The defluoridation mechanism can be elucidated through the XPS spectra analysis of Ce–Al–O/AC and Ce–Al–O/AC–F. Fig. 7(a) confirms the presence of Ce, Al, O, and C in the composite adsorbent, and the successful capture of fluoride ions, evidenced by the emergence of a new F 1s orbital peak appears at 686 eV after adsorption.[13] Fig. 7(b–e) displays the XPS spectra of F, Al, O, and Ce, respectively. In the F 1s XPS spectrum of Ce–Al–O/AC–F (Fig. 7(b)), two peaks at 685.55 eV and 686.50 eV correspond to Ce–F and Al–F respectively, and the higher relative area ratio of Al–F (71.92%) compared to Ce–F (28.08%) is attributed to the Al/Ce ratio of 14 : 3 in the material. Besides, the

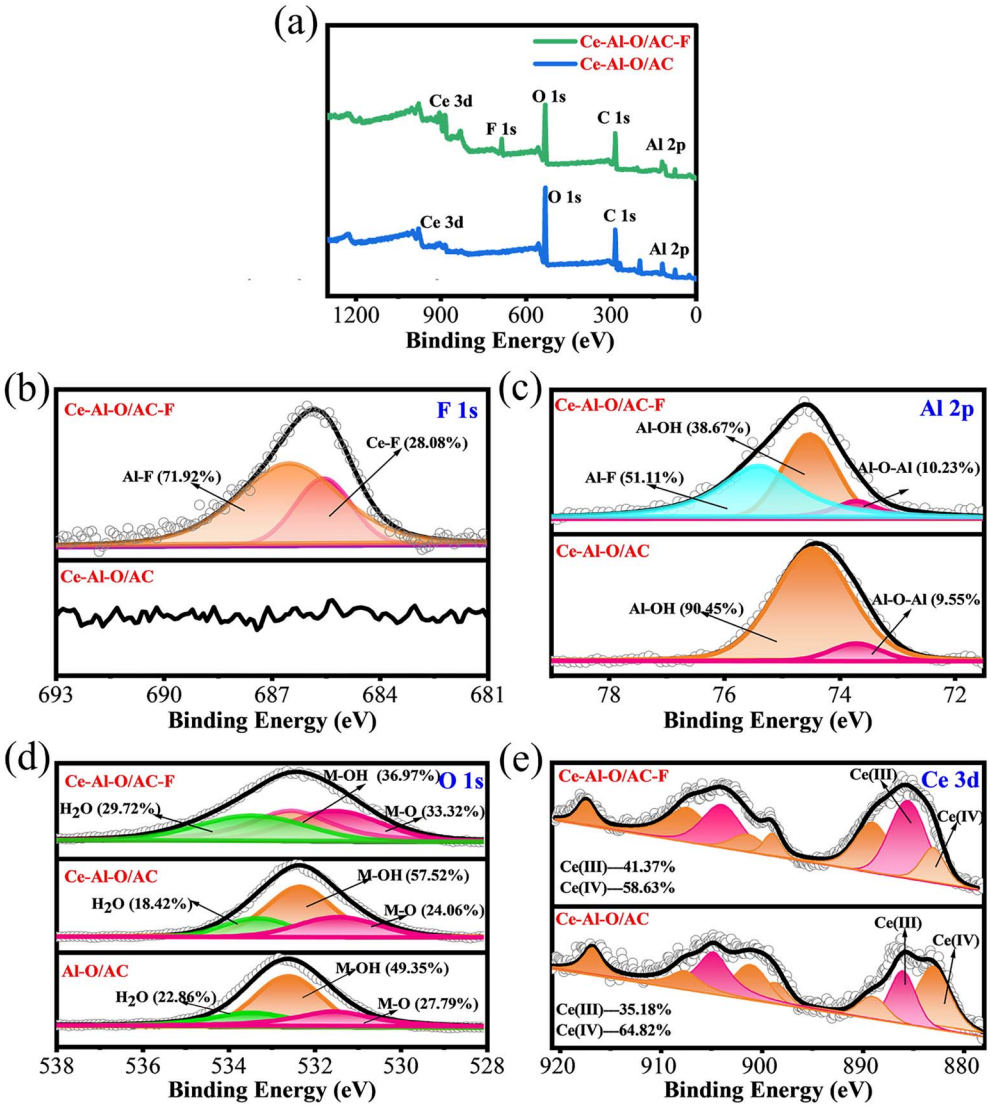

Fig. 7 (a) XPS spectra of Ce–Al–O/AC and Ce–Al–O/AC–F, (b) F 1s XPS spectra of Ce–Al–O/AC and Ce–Al–O/AC–F, (c) Al 2p XPS spectra of Ce–Al–O/AC and Ce–Al–O/AC–F, (d) O 1s XPS spectra of Al–O/AC, Ce–Al–O/AC and Ce–Al–O/AC–F, (e) Ce 3d XPS spectra of Ce–Al–O/AC and Ce–Al–O/AC–F.

binding energies of Ce–F and Al–F exceed that of the NaF peak (684.5 eV), illustrating that fluoride ions undergo complexation with Ce and Al.[38,53] The Al 2p spectra of Ce–Al–O/AC (Fig. 7(c)) exhibit two peaks at 73.7 eV and 74.45 eV, corresponding to Al–O and Al–OH, respectively. Moreover, the Al 2p spectra of Ce–Al–O/AC–F reveal a new peak at 75.4 eV attributed to Al–F, further corroborating the interaction between fluoride ions and aluminum in the composite adsorbent. In Fig. 7(d), the O 1s spectra of Ce–Al–O/AC can be classified into three peaks at 531.18, 532.43, and 533.3 eV, representing M–O, M–OH, and H_2O (where M denotes Ce and Al), respectively.[25] In particular, compared to the spectra of Ce–Al–O/AC, the relative area of M–OH decreases from 57.52% to 36.97% in Ce–Al–O/AC–F. It strongly indicates the participation of hydroxyl groups in defluoridation through the ion exchange process,[38] which is consistent with the FTIR results. Furthermore, the relative area of M–OH is larger in the spectra of Ce–Al–O/AC than Al–O/AC, which speculates that the doping of Ce–Al bimetallic increases the hydroxyl content of the adsorbent and exhibits better performance for fluoride removal. As shown in the Ce 3d spectra of Ce–Al–O/AC (Fig. 7(e)), the peaks at 916.80, 907.59, 901.04, 898.66, 888.90 and 882.90 eV are attributed to Ce(IV), the peaks at 904.77 and 885.94 eV are related to Ce(III).[38] As the Ce–Al–O/AC composite was synthesized *via* a hydrothermal process at 203 °C in a nitrogen atmosphere tube furnace. The exposure to high temperature and low oxygen partial pressures facilitated the desorption of oxygen from the CeO_2 surface into the gas phase, thereby generating intrinsic oxygen vacancies and releasing electrons, which subsequently reduce Ce(IV) to the Ce(III) oxidation state.[1] After fluoride adsorption, the binding energies of the Ce 3d XPS spectra slightly shift, which indicates that the hydroxyl groups on the surface of Ce participated in the fluoride adsorption.[25] Furthermore, the relative area of Ce(IV) is decreased from 64.82% to 58.63%, while the relative area of Ce(III) is increased from 35.18% to 41.37%. It indicates a slight change reemerged in the CeO_2 lattice, resulting in an increase number of activated oxygen vacancies (defects) and facilitating the reduction of Ce(IV) to Ce(III).[1] The elevated proportion of Ce(III) implies a higher density of active center sites for the reaction,[54] which in turn facilitates the formation of –OH groups on the surface, and subsequently promotes the efficiency of ion exchange with fluoride ions. These findings are in accordance with the other studies.[1,25,26]

To reach a further understanding of the adsorption mechanism, DFT calculations were performed to investigate the adsorption of F^- and OH^- on the surface of Ce–Al–O/AC as well as Al–O/AC, as shown in Fig. 8 and S6.† The highlighted adsorption energy (E_{ad}) can be described as follows:[55]

$$E_{ad} = E_{total} - E_{ion} - E_{sub} \quad (3)$$

where E_{total} is the total energy of the adsorbed configurations, E_{ion} and E_{sub} represent the total energies of adsorbed ion and substrate materials, respectively. From Fig. 8(a) and (b), the calculated E_{ad} (−6.71 eV) for F^- adsorbed on the top of Al–O/AC, which is more negative than the obtained E_{ad} (−5.82 eV) for OH^- adsorbed on Al–O/AC. The more negative E_{ad} value implies

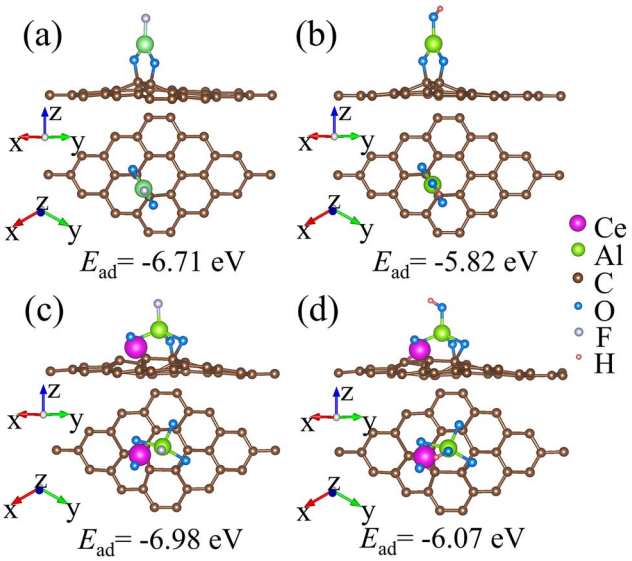

Fig. 8 The top and side views of absorption configurations for (a) F^- and (b) OH^- adsorbed on Al–O/AC. (c) F^- and (d) OH^- adsorbed on Ce–Al–O/AC. E_{ad} represents the adsorption energy.

the fact that Al–O/AC shows greater adsorption properties of F^- than OH^-. Moreover, from Fig. 8(c) and (d), the calculated E_{ad} (−6.98 eV) for F^- adsorbed on Ce–Al–O/AC, which is also more negative than the calculated E_{ad} (−6.07 eV) for OH^- adsorbed on Ce–Al–O/AC. These results reveal that Ce–Al–O/AC hold good adsorption performance for F^- than OH^-. Therefore, the more negative E_{ad} values for F^- adsorption indicate that ionic exchange from OH^- to F^- is likely to occur for both the Al–O/AC and Ce–Al–O/AC case. On the other hand, the calculated E_{ad} for F^- adsorbed on Ce–Al–O/AC is more negative than that of Al–O/AC, revealing that Ce–Al–O/AC possesses better fluoride absorption performance. Additionally, the energy difference of E_{ad} between F^- and OH^- is −0.89 eV for Al–O/AC and −0.91 eV for Ce–Al–O/AC, respectively, revealing that the replacing of OH^- with F^- is more easily to occur on the surface of Ce–Al–O/AC. Furthermore, as demonstrated by XRD, the Ce–Al oxides loaded on activated carbon exhibit structures where Ce oxide

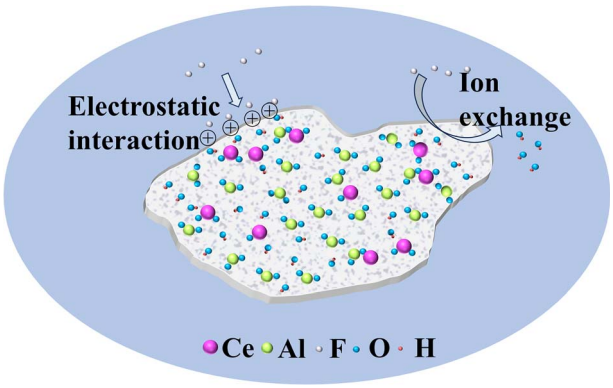

Fig. 9 Schematic of the mechanism of fluoride removal by Ce–Al–O/AC.

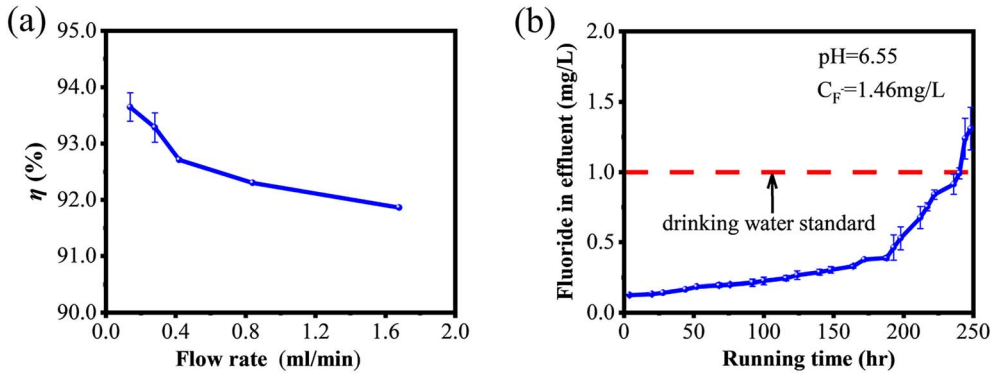

Fig. 10 (a) The defluorination rates of fixed-bed columns with the testing drinking water at different flow rates, (b) breakthrough profiles of defluoridation from fixed-bed columns with the testing drinking water.

and Al oxide are separately on the activated carbon. The possible adsorption forms of F^- and OH^- by these structures are depicted in Fig. S6.† In conjunction with Fig. S6,† further calculations reveal that the energy difference of E_{ad} between (a) and (d), (b) and (d), and (c) and (d) are −16.71 eV, −3.3 eV, and −4.42 eV, respectively, which are more negative than the energy difference of E_{ad} between F^- and OH^- for Al–O/AC. These phenomenons indicate that Ce–Al–O/AC demonstrates better fluoride removal performance by ion exchange between fluoride ions and hydroxyl groups than Al–O/AC, which is consistent with our experimental results.

Therefore, the results of the above experimental and theoretical analysis show that the mechanism of fluoride removal is mainly electrostatic interaction and ion exchange (shown in Fig. 9), involving the following chemical reactions:

$$\text{Ion exchange: (MO)–OH} + F^- \rightarrow \text{(MO)–F} + OH^- \quad (4)$$

$$\text{Electrostatic interaction: (MO)–OH} + H^+ + F^- \rightarrow \text{(MO)–OH}_2 - F \quad (5)$$

where, M = Ce^{4+}, Ce^{3+} and Al^{3+}.

3.6. Dynamic adsorption test and economic analysis

The viability of Ce–Al–O/AC for practical application depends on its efficacy in treating fluoridated drinking water and its economic feasibility. As depicted in Fig. 10(a), the defluoridation efficiency of fixed-bed columns exhibits a slight decline with increasing water treatment flow rate, yet consistently remains above 91%. This implies that the dynamic system has a rapid adsorption rate and strong resistance to fluctuations in water volume. Considering treatment efficiency and flow rate, subsequent tests on the fixed-bed columns were further conducted at a treatment flow rate of 0.42 mL min^{-1} to assess the potential fluoride removal capacity (Fig. 10(b)). Fig. 10(b) illustrates that the effluent fluoride concentration progressively increases with operational time. After 240 hours, the average effluent fluoride concentration approaches 1.0 mg L^{-1}, approximating the threshold for drinking water standard. Consequently, the effective treatment volume of drinking water is approximately 6048 mL. For a household of three with an annual drinking water consumption of 2 m^3, 1.0 kg of such adsorbent would be required. To evaluate the economic performance of Ce–Al–O/AC, the energy consumption and resource costs associated with its preparation (Table S8†) were calculated based on previous studies.[26] When Compared with the costs of conventional household water purifier cartridges (Table S9†), the total expense of utilizing Ce–Al–O/AC for treating 2 m^3 of drinking water amounts to £2.45, representing about 10% of the cost of water purifier cartridges and drastically reducing the water treatment cost. Therefore Ce–Al–O/AC emerges as a cost-effective and efficient adsorbent for practical drinking water defluoridation.

4. Conclusions

The Ce–Al–O/AC composite adsorbent, synthesized *via* the co-precipitation method, has been effectively applied to remediate fluoridated drinking water. Static adsorption studies reveal its superior defluoridation performance with a maximum sorption capacity of 31.65 mg g^{-1} at 298 K. The composite adsorbent maintains high efficiency across a wide pH range of 4–10, demonstrating its robustness for various environmental conditions. Phosphate anions were identified as an interference with the defluoridation process. The rapid defluoridation rate, achieving 94.8% of the equilibrium adsorption capacity within 15 minutes, underscores its potential for practical applications. The adsorption kinetics and isotherm data align well with the pseudo-second-order kinetic model and Langmuir isotherm model, respectively. The thermodynamic analysis confirms that the adsorption reaction is a spontaneous and endothermic process. Experimental and theoretical analysis indicate that electrostatic interactions and ion exchange as the primary mechanisms underlying the defluoridation by Ce–Al–O/AC.

The development of the Ce–Al–O/AC composite adsorbent provides an efficient and economical solution for fluoride removal from drinking water. The adsorbent's ability to function effectively over a wide pH range and its rapid defluoridation rate enhance its suitability for real-world applications. The economic analysis, demonstrating lower cost compared to

conventional drinking water purification methods, further emphasizes its potential for widespread adoption. Future research should focus on scaling up the production of Ce–Al–O/AC and evaluating its long-term performance in various drinking water conditions to fully realize its environmental and public health benefits.

Data availability

The authors confirm that the data supporting the findings of this study are available within the article [and/or its ESI†].

Conflicts of interest

The authors declare no competing financial interest.

Acknowledgements

This work is financially supported by the Young and middle-aged Scientific Research Project of Education Department of Fujian Province (Grant No. JAT241283), Natural Science Foundation of Fujian Province (Grant No. 2021J06011), and Fujian Provincial Key Laboratory of Pollution Control & Resource Reuse Open Project Fund.

References

1 U. S. Rashid, T. K. Das, T. S. Sakthivel, S. Seal and A. N. Bezbaruah, GO-CeO_2 nanohybrid for ultra-rapid fluoride removal from drinking water, *Sci. Total Environ.*, 2021, **793**, 148547.

2 R. Foroutan, R. Mohammadi, J. Razeghi, M. Ahmadi and B. Ramavandi, Amendment of Sargassum oligocystum biochar with $MnFe_2O_4$ and lanthanum MOF obtained from PET waste for fluoride removal: A comparative study, *Environ. Res.*, 2024, **251**, 118641.

3 I. Mukherjee and U. K. Singh, Exploring a variance decomposition approach integrated with the Monte Carlo method to evaluate groundwater fluoride exposure on the residents of a typical fluorosis endemic semi-arid tract of India, *Environ. Res.*, 2022, **203**, 111697.

4 C. F. Z. Lacson, M. C. Lu and Y. H. Huang, Chemical precipitation at extreme fluoride concentration and potential recovery of CaF_2 particles by fluidized-bed homogenous crystallization process, *Chem. Eng. J.*, 2021, **415**, 128917.

5 W. J. Xue, F. F. Zhang, W. D. Ding, K. F. Zhang and Q. W. Zhang, Enhanced removal of fluoride ions using lanthanum-doped coconut shell biochar in PVDF ultrafiltration membranes, *J. Hazard. Mater.*, 2024, **480**, 136393.

6 S. Singh, M. German, S. Chaudhari and A. K. Sengupta, Fluoride removal from groundwater using Zirconium Impregnated Anion Exchange Resin, *J. Environ. Manage.*, 2020, **263**, 110415.

7 Q. Li, Z. Zeng, L. Huang, S. J. Zhao, J. Yan, X. Y. Zhao, Z. X. Chen and H. G. Zhang, Depth analysis of the mechanism for fluoride removal by adsorption of schwertmannite: Experiments and theoretical calculations, *J. Mol. Liq.*, 2024, **401**, 124658.

8 W. Guo, H. F. Lin, H. X. Zhu, W. Mo, X. J. Su, J. L. Yang, S. J. Ma, J. P. Feng and M. Lei, Efficient removal of fluorine by carbon fiber supported Mg-Fe binary metal oxide composite adsorbent and mechanism analysis based on DFT, *Sep. Purif. Technol.*, 2024, **330**, 125320.

9 S. Nehra, S. Raghav and D. Kumar, Biomaterial functionalized cerium nanocomposite for removal of fluoride using central composite design optimization study, *Environ. Pollut.*, 2020, **258**, 113773.

10 J. Wen, S. Yang, L. Jiang, Y. Shi, Z. Huang, P. Li, H. Xiong, Z. Yu, X. Zhao, B. Xu, B. Wu, B. Sa and Y. Qiu, Accelerated discovery of high-performance small-molecule hole transport materials via molecular splicing, high-throughput screening, and machine learning, *J. Mater. Inf.*, 2025, **5**(3), 30.

11 S. Mandal, B. Panda, D. Mondal, J. Khatun, P. Dhak and D. Dhak, 3D flower-like zirconium magnesium oxide nanocomposite for efficient fluoride removal, *Environ. Sci. Pollut. Res.*, 2023, **30**, 119491–119505.

12 A. K. Tolkou, S. Trikalioti, O. Makrogianni, D. G. Trikkaliotis, E. A. Deliyanni, G. Z. Kyzas and I. A. Katsoyiannis, Magnesium modified activated carbons derived from coconut shells for the removal of fluoride from water, *Sustainable Chem. Pharm.*, 2023, **31**, 100898.

13 J. Song, Y. Yu, X. Han, W. Yang, W. Pan, S. Jian, G. Duan, S. Jiang and J. Hu, Novel MOF(Zr)-on-MOF(Ce) adsorbent for elimination of excess fluoride from aqueous solution, *J. Hazard. Mater.*, 2024, **463**, 132843.

14 J. Lin, T. Ban, T. Li, Y. Sun, S. Zhou, R. Li, Y. Su, J. Kasemchainan, H. Gao, L. Shi and G. Wang, Machine-learning-assisted intelligent synthesis of UiO-66(Ce): Balancing the trade-off between structural defects and thermal stability for efficient hydrogenation of Dicyclopentadiene, *MGE Adv.*, 2024, **2**(3), e61.

15 H. Liu, Z. Cui, Z. Qiao, X. An and Y. Wang, Machine learning-assisted prediction, screen, and interpretation of porous carbon materials for high-performance supercapacitors, *J. Mater. Inf.*, 2024, **4**(4), 16.

16 C. Zhang, S. Qin, H. Gao and P. Jin, High hydrogen evolution activities of dual-metal atoms incorporated N-doped graphenes achieved by coordination regulation, *J. Mater. Inf.*, 2024, **4**(1), 1.

17 G. Z. Kyzas, A. K. Tolkou, T. J. Al Musawi, N. Mengelizadeh, S. Mohebi and D. Balarak, Fluoride Removal from Water by Using Green Magnetic Activated Carbon Derived from Canola Stalks, *Water, Air, Soil Pollut.*, 2022, **233**, 424.

18 M. H. Dehghani, M. Farhang, M. Alimohammadi, M. Afsharnia and G. McKay, Adsorptive removal of fluoride from water by activated carbon derived from $CaCl_2$-modified Crocus sativus leaves: Equilibrium adsorption isotherms, optimization, and influence of anions, *Chem. Eng. Commun.*, 2018, **205**, 955–965.

19 S. Bakhta, Z. Sadaoui, U. Lassi, H. Romar, R. Kupila and J. Vieillard, Performances of metals modified activated

carbons for fluoride removal from aqueous solutions, *Chem. Phys. Lett.*, 2020, **754**, 137705.

20 G. Wendimu, F. Zewge and E. Mulugeta, Aluminium-iron-amended activated bamboo charcoal (AIAABC) for fluoride removal from aqueous solutions, *J. Water Process Eng.*, 2017, **16**, 123–131.

21 Y. X. Li, Y. J. Xiao, T. X. Lu, G. C. He, Z. X. Ding, D. L. Wang, P. Zhang and Y. L. Hu, MgO modified sucrose-derived porous carbon composite for fluoride adsorption, *Desalin. Water Treat.*, 2024, **319**, 100529.

22 D. Mohanta and M. Ahmaruzzaman, Bio-inspired adsorption of arsenite and fluoride from aqueous solutions using activated carbon@SnO_2 nanocomposites: Isotherms, kinetics, thermodynamics, cost estimation and regeneration studies, *J. Environ. Chem. Eng.*, 2018, **6**, 356–366.

23 T. T. Pang, T. S. A. Chan, Y. A. C. Jande and J. J. Shen, Removal of fluoride from water using activated carbon fibres modified with zirconium by a drop-coating method, *Chemosphere*, 2020, **255**, 126950.

24 N. V. Arteaga-Larios, K. J. Ramírez-Muñíz, L. A. Bernal-Jácome, M. S. Berber-Mendoza, A. S. Garzón-Pérez and I. Rodríguez, Forced hydrolysis synthesis of a lanthanum oxyhydroxide/hydroxide-incorporated adsorbent for fluoride adsorption, *Int. J. Environ. Sci. Technol.*, 2024, **22**, 2849–2866.

25 N. Musa, B. K. Allam, N. B. Singh and S. Banerjee, Investigation on water defluoridation *via* batch and continuous mode using Ce–Al bimetallic oxide: Adsorption dynamics, electrochemical and LCA analysis, *Environ. Pollut.*, 2023, **328**, 121639.

26 S. I. Alhassan, H. Y. Wang, Y. J. He, L. J. Yan, Y. X. Jiang, B. C. Wu, T. Wang, H. Y. Gang, L. Huang, L. F. Jin and Y. S. Chen, Fluoride remediation from on-site wastewater using optimized bauxite nanocomposite (Bx-Ce-La@500): Synthesis maximization, and mechanism of F^- removal, *J. Hazard. Mater.*, 2022, **430**, 128401.

27 J. B. Huo and G. C. Yu, Mesoporous cerium oxide-anchored magnetic polyhedrons derived from MIL-100(Fe) for enhanced removal of arsenite from aqueous solution, *J. Hazard. Mater.*, 2021, **415**, 125709.

28 K. T. Wang, H. Y. Lei, Y. Muhammad, F. Chen, F. Gao, Y. Z. Wei and T. Fujita, Controlled preparation of cerium oxide loaded slag-based geopolymer microspheres (CeO_2@SGMs) for the adsorptive removal and solidification of F^- from acidic waste-water, *J. Hazard. Mater.*, 2020, **400**, 123199.

29 S. Smidstrup, T. Markussen, P. Vancraeyveld, J. Wellendorff, J. Schneider, T. Gunst, B. Verstichel, D. Stradi, P. A. Khomyakov, U. G. Vej-Hansen, M. E. Lee, S. T. Chill, F. Rasmussen, G. Penazzi, F. Corsetti, A. Ojanperä, K. Jensen, M. L. N. Palsgaard, U. Martinez, A. Blom, M. Brandbyge and K. Stokbro, QuantumATK: an integrated platform of electronic and atomic-scale modelling tools, *J. Phys. Condens. Matter*, 2020, **32**, 015901.

30 M. J. van Setten, M. Giantomassi, E. Bousquet, M. J. Verstraete, D. R. Hamann, X. Gonze and G. M. Rignanese, The PSEUDODOJO: Training and grading a 85 element optimized norm-conserving pseudopotential table, *Comput. Phys. Commun.*, 2018, **226**, 39–54.

31 V. Blum, R. Gehrke, F. Hanke, P. Havu, V. Havu, X. G. Ren, K. Reuter and M. Scheffler, Ab initio molecular simulations with numeric atom-centered orbitals, *Comput. Phys. Commun.*, 2009, **180**, 2175–2196.

32 S. Grimme, J. Antony, S. Ehrlich and H. Krieg, A consistent and accurate *ab initio* parametrization of density functional dispersion correction (DFT-D) for the 94 elements H-Pu, *J. Chem. Phys.*, 2010, **132**, 154104.

33 Y. Shi, Y. Zhang, J. Wen, Z. Cui, J. Chen, X. Huang, C. Wen, B. Sa and Z. Sun, Interpretable machine learning for stability and electronic structure prediction of Janus III–VI van der Waals heterostructures, *MGE Adv.*, 2024, **2**, e76.

34 H. Liu, S. B. Deng, Z. J. Li, G. Yu and J. Huang, Preparation of Al-Ce hybrid adsorbent and its application for defluoridation of drinking water, *J. Hazard. Mater.*, 2010, **179**, 424–430.

35 W. Guo, H. Lin, H. Zhu, W. Mo, X. Su, J. Yang, S. Ma, J. Feng and M. Lei, Efficient removal of fluorine by carbon fiber supported Mg-Fe binary metal oxide composite adsorbent and mechanism analysis based on DFT, *Sep. Purif. Technol.*, 2024, **330**, 125320.

36 D. D. Bao, Z. W. Li, R. Tang, C. L. Wan, C. Zhang, X. J. Tan and X. Liu, Metal-modified sludge-based biochar enhance catalytic capacity: Characteristics and mechanism, *J. Environ. Manage.*, 2021, **284**, 112113.

37 S. Bose, T. Mukherjee and M. Rahaman, Simultaneous adsorption of manganese and fluoride from aqueous solution *via* bimetal impregnated activated carbon derived from waste tire: Response surface method modeling approach, *Environ. Prog. Sustainable Energy*, 2021, **40**, e13600.

38 Y. F. Wei, L. Wang and J. Y. Wang, Cerium alginate cross-linking with biochar beads for fast fluoride removal over a wide pH range, *Colloids Surf., A*, 2022, **636**, 128161.

39 G. I. Danmaliki and T. A. Saleh, Effects of bimetallic Ce/Fe nanoparticles on the desulfurization of thiophenes using activated carbon, *Chem. Eng. J.*, 2017, **307**, 914–927.

40 A. Dhillon, S. K. Soni and D. Kumar, Enhanced fluoride removal performance by Ce-Zn binary metal oxide: Adsorption characteristics and mechanism, *J. Fluorine Chem.*, 2017, **199**, 67–76.

41 X. He, J. Jiang, Z. N. Hong, X. Y. Pan, Y. Dong and R. K. Xu, Effect of aluminum modification of rice straw-based biochar on arsenate adsorption, *J. Soils Sediments*, 2020, **20**, 3073–3082.

42 M. Gao, W. Wang, M. B. Cao, H. B. Yang and Y. S. Li, Hierarchical hollow manganese-magnesium-aluminum ternary metal oxide for fluoride elimination, *Environ. Res.*, 2020, **188**, 109735.

43 X. Q. Zhang, Y. L. Qi, Z. H. Chen, N. N. Song, X. Li, D. J. Ren and S. Q. Zhang, Evaluation of fluoride and cadmium adsorption modification of corn stalk by aluminum trichloride, *Appl. Surf. Sci.*, 2021, **543**, 148727.

44 A. Mullick and S. Neogi, Acoustic cavitation induced synthesis of zirconium impregnated activated carbon for

effective fluoride scavenging from water by adsorption, *Ultrason. Sonochem.*, 2018, **45**, 65–77.

45 S. Ghosh, R. Prabhakar and S. R. Samadder, Performance of γ-aluminium oxide nanoparticles for arsenic removal from groundwater, *Clean Technol. Environ. Policy*, 2018, **21**, 121–138.

46 A. N. Wagassa, A. Bansiwal, T. A. Shifa and E. A. Zereffa, Ce^{4+}-Substituted Ni–Al mixed oxide: fluoride adsorption performance and reusability, *RSC Adv.*, 2024, **14**, 1229–1238.

47 K. Singh, D. H. Lataye and K. L. Wasewar, Removal of fluoride from aqueous solution by using bael (Aegle marmelos) shell activated carbon: Kinetic, equilibrium and thermodynamic study, *J. Fluorine Chem.*, 2017, **194**, 23–32.

48 R. Wang, D. Wang, W. Peng, J. Zhang, J. Liu, Y. Wang and X. Wang, Removal of F^- from water by magnetic floriform magnesium zirconium hydrotalcite-like material doped with Fe_2O_3 and ZrO_2, *Desalination*, 2022, **544**, 116142.

49 T. Wu, L. L. Mao and H. Z. Wang, Adsorption of fluoride from aqueous solution by using hybrid adsorbent fabricated with Mg/Fe composite oxide and alginate *via* a facile method, *J. Fluorine Chem.*, 2017, **200**, 8–17.

50 S. Huang, X. Zhang, L. Wang, D. Li, C. Zhang, L. Yang, Q. He and B. Gao, Enhanced water defluoridation using ion channel modified hydroxyapatite: Experimental, mechanisms and DFT calculation, *Appl. Surf. Sci.*, 2023, **615**, 156351.

51 C. Jia, J. Wang, H. Wang, S. Zhu, X. Zhang and Y. Wang, Performance and mechanism of La-Fe metal-organic framework as a highly efficient adsorbent for fluoride removal from mine water, *J. Environ. Sci.*, 2024, **139**, 245–257.

52 J. L. Tang, J. L. Zhao, S. X. Wang, L. B. Zhang, M. H. Zhao, Z. Huang and Y. T. Hu, Pre-modification strategy to prepare a novel Zr-based MOF for selective adsorption of Palladium(II) from solution, *Chem. Eng. J.*, 2021, **407**, 127223.

53 L. P. Mei, C. Y. Peng, H. H. Qiao, F. Ke, J. Liang, R. Y. Hou, X. C. Wan and H. M. Cai, Enhanced removal of fluoride by zirconium modified tea waste with extrusion treatment: kinetics and mechanism, *RSC Adv.*, 2019, **9**, 33345–33353.

54 J. Seo, J. Moon, J. H. Kim, K. Lee, J. Hwang, H. Yoon, D. K. Yi and U. Paik, Role of the oxidation state of cerium on the ceria surfaces for silicate adsorption, *Appl. Surf. Sci.*, 2016, **389**, 311–315.

55 W. Q. Xia, W. Hu, Z. Y. Li and J. L. Yang, A first-principles study of gas adsorption on germanene, *Phys. Chem. Chem. Phys.*, 2014, **16**, 22495–22498.